Taylor & Francis
Taylor & Francis Group

RESEARCH ARTICLE

🔓 OPEN ACCESS   Check for updates

Binding kinetics of quaternary ammonium ions in Kcv potassium channels

Tobias Korn[a], Ulf-Peter Hansen[b], Tobias Sebastian Gabriel[a], Oliver Rauh[a], Nils Drexler[c], and Indra Schroeder 🆔[a,c]

[a]Plant Membrane Biophysics, Technische Universität Darmstadt, Darmstadt, Germany; [b]Department of Structural Biology, Christian-Albrechts-University, Kiel, Germany; [c]Physiology II, University Hospital Jena, Friedrich Schiller University, Jena, Germany

ABSTRACT

Kcv channels from plant viruses represent the autonomous pore module of potassium channels, devoid of any regulatory domains. These small proteins show very reproducible single-channel behavior in planar lipid bilayers. Thus, they are an optimum system for the study of the biophysics of ion transport and gating. Structural models based on homology modeling have been used successfully, but experimental structural data are currently not available. Here we determine the size of the cytosolic pore entrance by studying the blocker kinetics. Blocker binding and dissociation rate constants ranging from 0.01 to 1000 ms^{-1} were determined for different quaternary ammonium ions. We found that the cytosolic pore entrance of Kcv$_{NTS}$ must be at least 11 Å wide. The results further indicate that the residues controlling a cytosolic gate in one of the Kcv isoforms influence blocker binding/dissociation as well as a second gate even when the cytosolic gate is in the open state. The voltage dependence of the rate constant of blocker release is used to test, which blockers bind to the same binding site.

Introduction

Viral Kcv (K$^+$ channel from chlorella virus) channels are optimum candidates for the study of conduction and gating mechanisms in the pore of potassium channels. Their small size prevents the interference from regulatory domains and provides results of high reproducibility [1]. There are up to five gating processes already described in these autonomous pores in the range of hundreds of milliseconds to microseconds, which can be kinetically well separated [2,3]. The existence of >80 isoforms in the Kcv family with different properties can serve as a guideline for mutational studies [1,2,4–6]. These benefits of Kcv channels greatly facilitate the determination of molecular parameters such as voltage-dependent ion distribution in the selectivity filter [3,7] and an unusual mechanism for the cytosolic gate in Kcv$_S$ [2].

Currently, no experimental structures for Kcv channels are available. Successful MD (Molecular Dynamics) simulation studies and 3D RISM (3D reference interaction site model) calculations have been done with structural models based on homology modeling and extensive refinements [2,7–9].

The selectivity filter of Kcv channels conforms with the canonical filter structure of the K$^+$ channel family, while the cytosolic gate does not. Therefore, it is desirable to have independent experimental structural constraints for this region. Thus, one issue of this work is the determination of the diameter of the cytosolic pore entrance (CPE).

To this end, we use small molecules binding inside ion channel pores and blocking their conductance. The study of this process has often been used for several purposes. In pharmacologically motivated studies, the understanding of the blocking mechanism supports the development of more specific and more effective drugs. Blocker accessibility studies are often used to identify the gate of a channel. In MthK channels, it has been verified in this way that the voltage- and calcium-controlled gate is in the selectivity filter [10,11]. Also for K2P channels, the absence of a cytosolic bundle-crossing gate has been demonstrated with blockers [12].

Here we use the kinetics of blocking by six different quaternary ammonium blockers (QAs) applied to Kcv$_{NTS}$ for the determination of the

accessible diameter of the CPE. In addition, the comparison with Kcv_S was used for the question whether the cytosolic gate in this isoform influences blocker access also in the open state. Kcv_S is less suitable for the determination of the diameter of the CPE because the blocking effect is too small for the reliable determination of the rate constants of blocking at higher negative voltages.

QAs of different sizes are often used to map the diameter of the cytosolic pore entrance (CPE) and the cavity. Due to their physical similarity to hydrated alkali metal ions, QAs ubiquitously block potassium (K^+) channels from the cytosolic side [13,14] by binding in the aqueous cavity at or near the dehydration site, where the K^+ ions strip off their water shell prior to entering the selectivity filter [15]. Early studies concluded that the path between the cytosol and the binding site in the squid axon K^+ channel must be at least 9 Å [13] or 12 Å [16] wide. Studies considering the individual on- and off-rates of the blockers as an alternative or in addition to the apparent dissociation constant provide a more detailed picture on the pore accessibility [17]. In some of these studies, a sudden steep drop (by about a factor of 30) in the on-rate between two QAs of different sizes was interpreted as an indirect measure for the diameter of the CPE [18].

For Kcv_{NTS} in this study, the accessibility of blockers to their binding site shows that the diameter is more than 11 Å, similar to values found also for other channels with an open bundle crossing [12,17,19].

The second question deals with the kind of mechanisms influencing blocking kinetics. Kcv_S and Kcv_{NTS} share about 90% sequence identity but differ in the presence (Kcv_S) or absence (Kcv_{NTS}) of the aforementioned cytosolic gate, which in Kcv_S involves the movement of a phenylalanine side chain [2]. We found that there is a significant difference in the binding and release kinetics for QAs even in the open state between the two channel isoforms. Via mutations at the cytosolic gate, we disprove the assumption that the decrease in the rate constant of blocker binding occurring also in the open state of the inner gate in Kcv_S is caused by diffusion limitation due to narrowing of the pathway by the side chain of F78. In the case of blocker release, the hypothesis of trapping is at least weakened. Instead, it is concluded

that the hydrophobicity and/or conformation of the microenvironment at the binding is modified by the residues controlling the gate. This is supported by the finding that part of this microenvironment also influences a second component of the intrinsic sub-millisecond gating at positive voltages.

This topic is of general importance since also other channels have aromatic side chains, which are facing the channel cavity such as the NaK2K channel [20] and Eag1 [21]. In CNG channels, narrowing of the central gate in the cavity is controlled by cGMP binding and also involves a phenylalanine [22].

Materials and methods

Mutagenesis, protein expression, and purification

The genes encoding for Kcv_{NTS} and Kcv_S were cloned into the pEXP5-CT/TOPO vector (Invitrogen) in previous works [2,23]. A stop codon inserted directly upstream of the coding sequence for the 6×His-tag in the plasmid allows for expression of the native channel proteins. Point mutations were introduced by site-directed mutagenesis using a protocol based on the method described in [24]. All constructs were sequenced by Microsynth Seqlab prior to expression.

For channel expression, an *in vitro* reaction (Expressway™ Mini Cell-Free Expression System, Invitrogen) was used. MSP1D1-His DMPC nano-discs (16 μM, Cube Biotech), containing multiple His tags, were added to the expression mixture. Purification was done on a 0.2 mL HisPur™ Ni-NTA spin column (ThermoFisher Scientific) following the manufacturer's instructions with one change in the protocol: Neither the washing nor the elution solutions contained salts, only imidazole. This improves the reconstitution efficiency into the bilayer [25].

Lipid bilayer experiments

Vertical planar lipid bilayer experiments were performed at room temperature (20–25°C) as described previously [23]. Briefly, 1,2-diphytanoyl-*sn*-glycero-3-phosphocholine (DPhPC, Avanti Polar Lipids) membranes were formed using the pseudo-painting

/air bubble technique [26] or the monolayer folding technique [27]. The purified channel-nanodisc complexes were diluted with 250 mM imidazole by a factor of 10^4 to 10^5, and 1–3 µl of the dilution was added directly to the bilayer in the *trans* compartment with a bent microliter syringe.

Recordings were done in symmetrical 100 mM KCl, 10 mM HEPES, adjusted to pH 7.0 with KOH. Channel orientation was verified utilizing the known asymmetry of the apparent IV curves of Kcv channels [28]. The *trans* compartment was grounded, and voltages were applied to the *cis* compartment. Positive currents in the graphs correspond to outward currents in the *in vivo* situation.

Constant voltages between +160 mV and −160 mV in steps of 20 mV were applied for 1 to 5 minutes. Currents were measured in voltage-clamp mode via Ag/AgCl electrodes connected to a patch-clamp amplifier (L/M-EPC-7, List-Medical, or Axopatch 200B, Molecular Devices), filtered with a 1-kHz 4-pole Bessel filter and digitized with a sampling frequency of 5 kHz (LIH 1600, HEKA Elektronik). The software Patchmaster (HEKA Elektronik) was used to control voltage protocols and record the currents. Currents recorded at constant voltage after the capacitive artifact following each voltage jump were analyzed. Blocker concentration was changed by replacing an appropriate amount of the solution with a stock solution of the respective QA-chloride in the *cis* (= cytosolic) chamber and gentle but thorough mixing with a 1 mL pipette. All blocker stock solutions contained 100 mM KCl and 10 mM HEPES. pH was adjusted to 7.0 with KOH.

Abbreviation of blocker names: TMA = tetramethylammonium, TEA = tetraethylammonium, TPrA = tetrapropylammonium, TBA = tetrabutylammonium, TPeA = tetrapentylammonium and THxA = tetrahexylammonium.
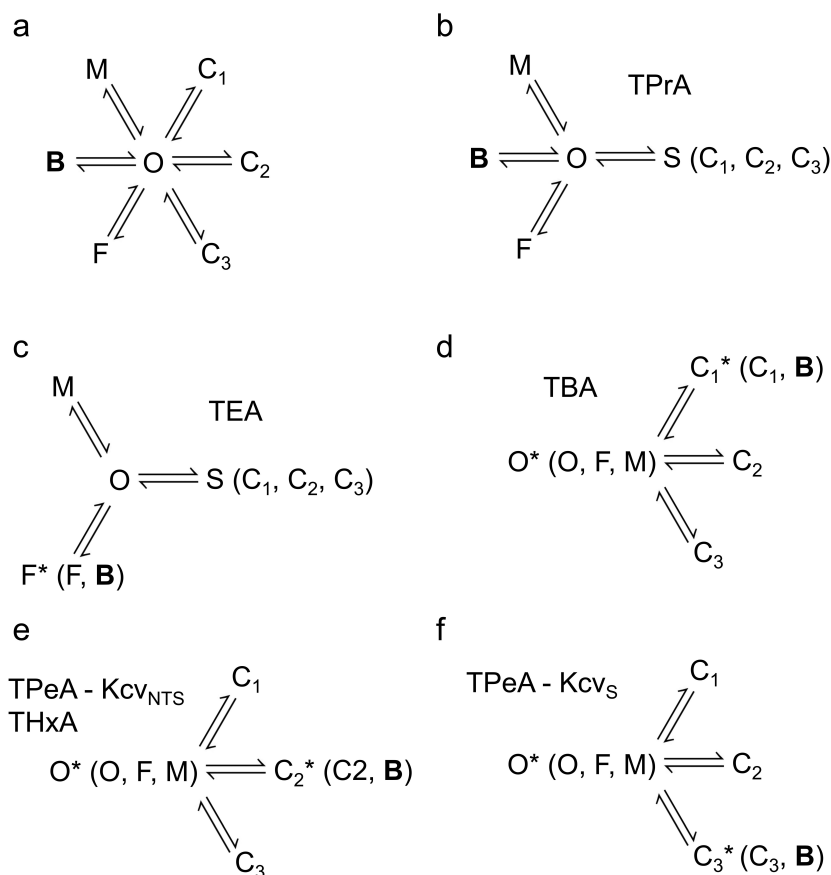
Different versions of the same Markov model for the determination of the rate constants of blocking

Figure 1a shows the complete Markov model including blocking and intrinsic gating, which holds for all experiments. From previous investigations [2,7,29], four (Kcv$_{NTS}$) to five (Kcv$_S$) closed states (F ("fast"), M ("medium"), C_1-C_3) and one open state (O) of intrinsic gating are known. C_3 occurs only in Kcv$_S$, but not in Kcv$_{NTS}$. The connection of the blocked state B solely to the open state is justified by the fact that in our steady-state recordings we can measure only those rate constants of blocking during the open state of the channel. Note that we do not exclude an additional closed-state block, however this would not be observable in our experiments. Further details on this argument and a discussion that a closed-state block is unlikely to significantly distort the results for the open-channel block are provided in a previous paper [7]. The wide temporal range of blocking kinetics for the different blockers requires two different methods of analysis (dwell-time analysis and fitting of current amplitude histograms) with different temporal resolution. Consequently, different versions of the full Markov model are used to account for the limitations of the two methods.

For the analysis of individual blockers, some of the states in Figure 1a are merged into a representative state to avoid overfitting when the data analysis cannot kinetically separate them. If the blocking events are so fast that they cannot be resolved by full open-closed transitions, they cause excess noise [30–32] of the open-channel current (Figure 3a, below). In this case, they have to be evaluated by fits of amplitude histograms with extended beta distributions (Figure S1 [32,33]). This method cannot distinguish between the slow intrinsic closed states since the related gating events cause equal contributions to the shape of the amplitude histograms. Thus, C_1 – C_3 are merged into one representative slow state S, resulting in the 5-state model used for TPrA (Figure 1b) already previously described [7]. In addition, extended beta distribution analysis faces the same principal problem as dwell-time analysis: If two states have the same average dwell time, they cannot be distinguished. Therefore, state B of the TEA data is furthermore merged with the very short closed state F (Figure 1c) since their dwell times are similar (*i.e.* k_{off} is in a similar range as k_{FO} (Figure S3). For the definition of the rate constants, see legend of Figure 1).

For the slow blockers, we use dwell time analysis. Thus, C_1–C_3 remain separated in the model. Instead, the short closed states M and F and the open state O are merged into an apparent open state O* (Figure 1d–f), since they cannot be distinguished by this method. Furthermore, for each

a

M C_1

$B \rightleftharpoons O \rightleftharpoons C_2$

F C_3

b

M   TPrA

$B \rightleftharpoons O \rightleftharpoons S\ (C_1, C_2, C_3)$

F

c

M   TEA

$O \rightleftharpoons S\ (C_1, C_2, C_3)$

$F^*\ (F, \mathbf{B})$

d

TBA $C_1^*\ (C_1, \mathbf{B})$

$O^*\ (O, F, M) \rightleftharpoons C_2$

C_3

e

TPeA - Kcv_{NTS}
THxA C_1

$O^*\ (O, F, M) \rightleftharpoons C_2^*\ (C2, \mathbf{B})$

C_3

f

TPeA - Kcv_S C_1

$O^*\ (O, F, M) \rightleftharpoons C_2$

$C_3^*\ (C_3, \mathbf{B})$

Figure 1. Markov models used for the fitting of the blocking kinetics. (a) The full Markov model with all states as known so far from previous studies [2,3,29] supplemented by the blocked state B. The states C_1, C_2 and C_3 belong to slow gating with dwell times longer than a millisecond, with C_3 occurring only in Kcv_S due to its cytosolic gate [2]. These states can be analyzed by a jump detector and dwell time analysis. F and M belong to fast gating (dwell-time in F about 5 μs) and medium gating (dwell-time in M is voltage-dependent ranging between 150 μs to 40 μs) [3]. (b, c) The models used for the analysis of fast blockers. C_1 - C_3 cannot be resolved by the beta distribution analysis and are merged into S ("slow"). (c) For TEA, B has a similar dwell time as F, so the two states cannot be kinetically separated. (b) for TPrA, this separation is possible [7]. (d,e,f) in the experiments with slow blockers, the dwell time in B coincides with one of the slow states C_1 - C_3. Thus, only two (Kcv_{NTS}) or three (Kcv_S) closed states are detected in the dwell time histograms. The inclusion of B is identified by concentration dependence. O,F,M are merged into an apparent open state O^*. Definition: The rate constant of the transition from a state X to a state Y is called k_{XY}. k_{BO} as the rate constant of blocker dissociation is also called k_{off}.

slow blocker, the dwell time of the blocked state B overlaps with one of the closed states, depending on the blocker and channel isoform. When B is merged with one of the closed states, this leads to a state C_1^*, C_2^* or C_3^*. The decision, which one includes B, is made by inspecting the dependency of the individual state occupancies on blocker concentration (Figures 6 to 8, below and Figure S4).

Analysis of fast blockers by extended beta distributions

As mentioned above, kinetics and blocking faster than the bandwidth of the recording set-up and the associated true open channel current I_{true}, which is also obscured by the filtering, have to be analyzed by fitting amplitude histograms with extended beta distributions [29,32] exploiting the open-channel excess noise [30,31]. Briefly, the program generates simulated time series [33,34] of single-channel current for the generation of the theoretical amplitude histogram, which is then fitted to the measured one by a simplex algorithm [35] by varying I_{true} and the rate constants of the Markov model (Figure 1b,c). The simulation and fitting algorithms and fitting strategies have been published elsewhere [32–34,36]. It is important to note that the simulation is done in continuous

time and includes Gaussian noise of the same magnitude as the experiment and a digital representation of the jump-response of the 4th-order Bessel filter used for the experiments. A more detailed description of the fit algorithm and examples of fits (Figure S1) are given in the Supplement.

Since this algorithm does not detect individual events, no precise minimal event length can be given. We estimated previously that gating about 100–500-fold faster as the filter frequency (1kHz in this work) can still reliably be quantified at SNR comparable to those in this study [32]. The temporal resolution depends on the deviation of the open peak from the Gaussian distribution of the baseline noise [37].

Analysis of slow blockers with dwell-time histograms

Open and closed dwell-time histograms of the single-channel recordings with slow blockers were calculated with an 8th-order Hinkley detector [38]. Briefly, the experimenter sets the current values for the baseline and the open channel, and the algorithm calculates a cumulative test value g_t from the raw data, counting only those data points which cross the halfway line between the closed and open level. When g_t reaches the threshold, which is set according to the noise level, a jump is detected [38]. Not considering filtering of the data, the approximate minimal detectable event length in sampling intervals is about $t_{res} = 22/SNR^2 = 4.4\,ms/SNR^2$ (Figure 5 in [38]), where SNR is the signal-to-noise-ratio. For dwell time analysis, only ±60 and ±100 mV were used; the SNR was at least 10. Consequently, the limiting factor for the event length is here the four-pole Bessel filter of 1 kHz, which has a rise time of about 400 μs. During the subsequent analysis of the resulting dwell-time histograms, we consider only events longer than 1 ms. For a more detailed description of these estimations, see [38,39]. Blockers that are faster than 1 ms are analyzed with extended beta distributions.

The resulting lifetimes were grouped into bins with exponentially increasing width. The theoretical probability density function of the open and closed lifetimes can be expressed as a sum of exponential functions, converted to match the exponential binning. The expected number N_i of events in the i-th bin with bin width Δt_i is

$$N_i = N \cdot \left(\sum_{j=1}^{n} a_j \cdot e^{-\frac{t_i}{\tau_j}} \left(e^{\frac{\Delta t_i}{\tau_j}} - 1 \right) \right). \qquad (1)$$

For open-time histograms $n = 1$ was used, for closed-time histograms $n = 2$ or 3. The time constants τ_j and the amplitude factors a_j describe the rate constants of the employed Markov model [40]. N denotes the total number of events. Due to the limited temporal resolution of the experimental setup, a notable number of short closed events associated with C_1 were missed by the jump detector. This results in an overestimation of the mean open lifetime τ_O. Therefore, a simple missed events correction was applied as described in [2].

Individual probabilities of the closed states C_j and the open state O were calculated by

$$P(C_j) = \frac{a_{C_j} \cdot \tau_{C_j}}{\tau_O + \sum_{j=1}^{n} a_{C_j} \cdot \tau_{C_j}} \quad \text{and}$$

$$P(O) = \frac{\tau_O}{\tau_O + \sum_{j=1}^{n} a_{C_j} \cdot \tau_{C_j}} \qquad (2a, b)$$

Since all closed states are directly connected to the open state (Figure 1), the rate constants could be calculated directly from the time constants and amplitude factors:

$$k_{C_jO} = \frac{1}{\tau_{C_j}} \quad \text{and} \quad k_{OC_j} = \frac{a_{C_j}}{\tau_O} \qquad (3a, b)$$

Dwell time fits were done with Matlab (MathWorks).

Supplementary material

The Supplementary Material contains additional figures and two tables. Figure S1: Fits of amplitude histograms with and without blocker. Figure S2: Example of time series, IV curves and open probabilities for the blocking experiments on Kcv$_S$. Figure S3: Blocking kinetics for TEA. Figure S4: Identification of the blocked state for TBA and THxA. Figure S5: Block by TPrA does not affect the OM-gating k_{OM} in all investigated constructs. Figure S6: Block by TBA does not affect the k_{OM} in Kcv$_{NTS}$. Figure S7: No effect of mutations on I_{true}. Table S1: Rate constants for the example fits in Figure S1. Table S2: Products of rate constants.

Results and discussion

Dependence of current and open probability on blocker size in Kcv$_{NTS}$

To measure the effect of blockers with different sizes, mono-cationic quaternary ammonium ions (QAs) with increasing size from TMA to THxA (Figure 2b) were applied to the cytosolic side of the viral K$^+$ channel Kcv$_{NTS}$.

Figure 3a shows representative single-channel recordings from Kcv$_{NTS}$ in DPhPC bilayers in symmetric 100 mM KCl at blocker concentrations close

to the respective apparent K$_D$s. All blockers show an increasing effect at positive voltages. The blocking kinetics become slower with increasing blocker size, as illustrated in Figure 3a.

The small blockers (TMA, TEA, and TPrA) cause a block, which is faster than the bandwidth of the recording. Averaging over the fast events by the 1-kHz low-pass filter leads to a reduction of the apparent current I_{app} (Figure 3bii–iv). The larger QAs (TBA, TPeA, and THxA) block slower, leading to a decrease in P_O (Figure 3cv–vii). An exception is TEA,
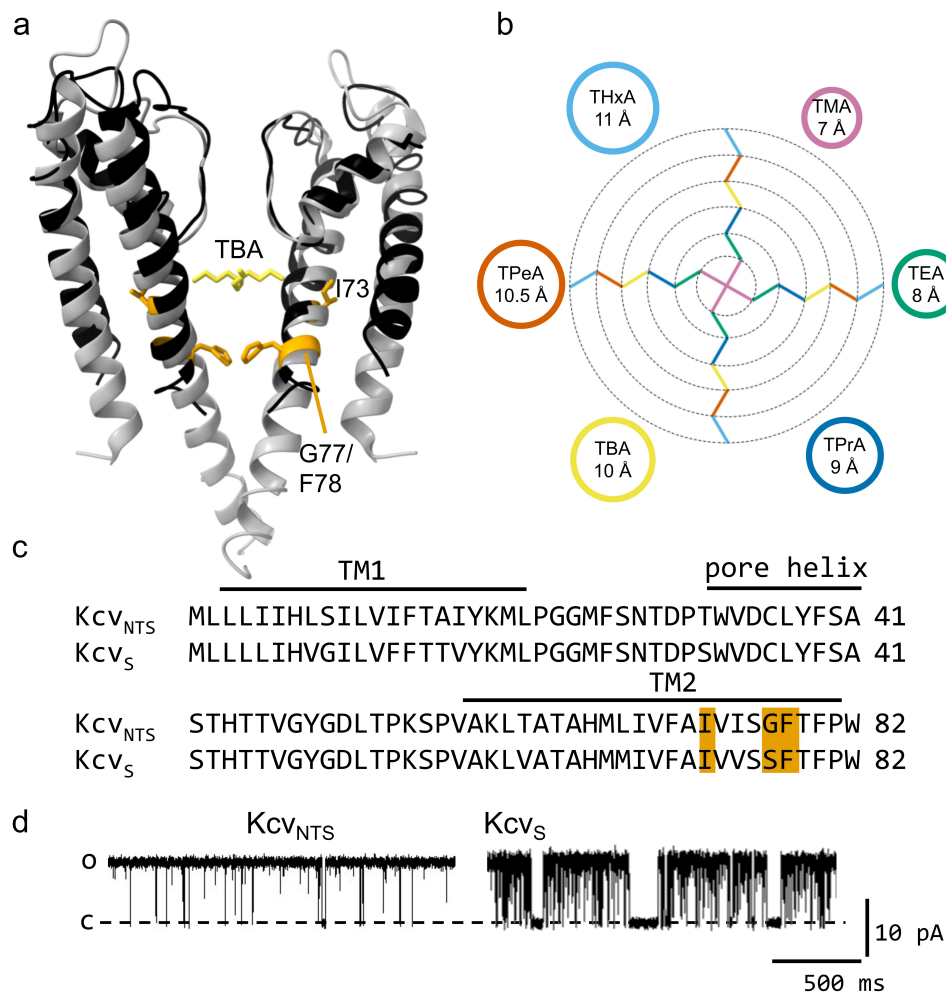
Figure 2. (a) Comparison of the structure of a homology model for Kcv$_{NTS}$ and the structure of the TBA@KcsA complex (pdb code 2HVK), which is used as an illustration of the location of the blocker [41]. Two monomers of the KcsA channel are shown in gray, the TBA ion (yellow) is located inside the cavity. The homology model of Kcv$_{NTS}$ on the template structure of KirBac1.1 (1P7B) calculated with Swissmodel [42] is shown in black with the amino acids discussed in this work highlighted in orange. Structures drawn with UCSF chimera [43]. (b) size of quaternary ammonium blockers (QAs), as estimated by [44]. The colors of the alkyl chains refer to the circles with the same color. The same accessible color palette ([45] and https://www.accessiblecolorpalette.com/, accessed June 2024) for the blockers is used in all figures in this work. (c) Sequence alignment of Kcv$_{NTS}$ and Kcv$_S$. Residues I73, G/S77 and F78 are highlighted in orange. (d) Representative single-channel traces of Kcv$_{NTS}$ and Kcv$_S$ at +120 mV in a DPhPC membrane in 100 mM KCl.
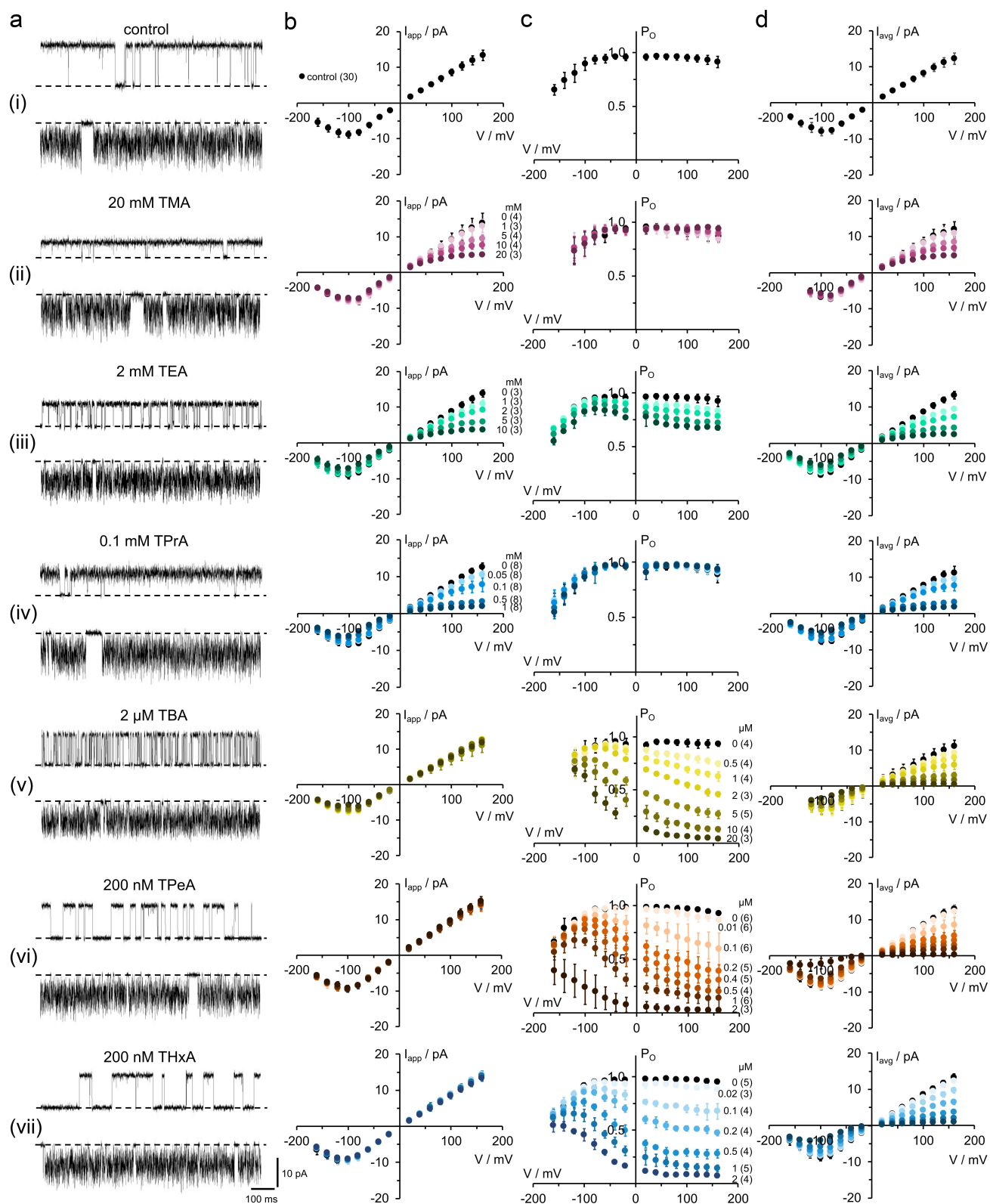
Figure 3. Blocking properties of Kcv$_{NTS}$ by cytosolic QAs. (a) Single-channel fluctuations in DPhPC bilayers in symmetric 100 mM KCl without and with different QAs recorded at +120 mV (upper traces) and −120 mV (lower traces). The closed channel is indicated by a dashed line. The blocker concentrations are given above the traces. (b) Apparent single-channel channel I_{app}/V-relations without (black) and with (colored) blocker, concentrations indicated at the curves in either (b) or (c). (c) Apparent open probabilities and (d) time averaged I_{avg}/V relations with $I_{avg} = I_{app} \cdot P_0$. Mean ± s.D., number of independent recordings is indicated in brackets.

which has two effects, one on I_{app} and one on P_0 (Figure 3biii,ciii). The increase in open-channel noise caused by the small blockers is easier to see in the time series at positive voltages in Figure 3a, since at negative voltages, it is mixed with the noise originating from fast intrinsic gating [3] seen in the control (Figure 3ai). The decrease in P_O caused by the larger blockers is indicated by the long sojourns at the baseline at positive voltages. Fast and slow blockers have similar effects on I_{avg}, the current obtained from averaging over the whole time series (Figure 3d).

To study the influence of the inner gate region on the block, the same experiments as in Figure 3 were also performed with the closely related channel Kcv_S and selected blockers (TEA, TPrA, TBA, TPeA, Figure S2). Fewer blockers were applied here, because Kcv_S was used only for studying the effect of the cytosolic gate (Figure 2a,c) and not the determination of the diameter of the CPE. Qualitatively, the results with Kcv_S were very similar to those of Kcv_{NTS} with a voltage-dependent block whose kinetics slow down with the size of the blocker.

The dependence of K_D on blocker size in Kcv_{NTS} and Kcv_S

For a more quantitative description, the apparent dissociation constants K_D were determined from concentration response curves (Figure 4a–d). Depending on the kinetics, the inhibition (Inh_{exp}) was calculated from the ratio of I_{app} (TMA, TPrA), I_{avg} (TEA) or P_O (TBA, TPeA, and THxA) with and without blocker (Eq. 4):

$$Inh_{exp} = 1 - \frac{I_{app,B}}{I_{app}},$$

$$Inh_{exp} = 1 - \frac{P_{O,B}}{P_O},$$

$$Inh_{exp} = 1 - \frac{I_{avg,B}}{I_{avg}} \quad (4a, b, c)$$

The subscript B indicates the experimental parameters determined with the blocker, the absence of this notation the control without blocker. The Hill equation (Eq. 5) with a fixed Hill coefficient of 1 leads to a satisfactory fit in all cases (Figure 4a–d).
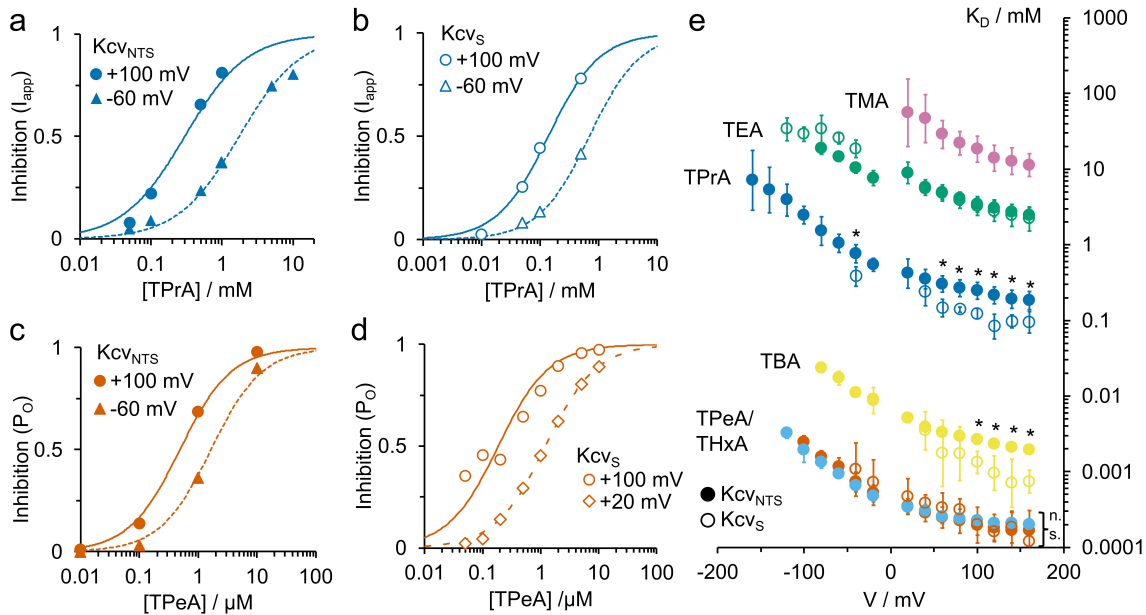
Figure 4. Representative concentration response curves of inhibition Inh_{exp} for (a,b) TPrA (9 Å diameter) and (c,d) TPeA (10.5 Å) in (a, c) Kcv_{NTS} and in (b,d) Kcv_S as obtained from the data in Figure 3 and Figure S2, respectively. Fit with Eq. 5. (e) Voltage dependence of apparent K_D (as obtained from fits like those in Figure 4a–d) for the different blockers in Kcv_{NTS} (filled circles) and Kcv_S (open circles). TMA: purple, TEA: green, TPrA: dark blue, TBA: yellow, TPeA: light blue, THxA: orange. *: At these voltages, the K_D for TPrA and TBA differ significantly from each other in Kcv_{NTS} and Kcv_S. "n.s.:" The K_D for TPeA (Kcv_{NTS} and Kcv_S) and TPeA (Kcv_{NTS}) do not differ significantly at any voltage. One-parameter ANOVA with threshold $p = 0.05$.

$$Inh = \frac{c}{K_D + c} \qquad (5)$$

with c = concentration of the blocker. Not all experiments reached saturation, but the range is sufficient to determine the apparent dissociation constant K_D, assuming maximum inhibition $Inh_{max} = 1$. K_D values for both channel isoforms at various voltages are shown in Figure 4e.

The K_D strongly declines with blocker size. For the largest two blockers (TPeA and THxA), K_D becomes independent of blocker size, as confirmed by a one-way ANOVA test for $p < 0.05$. All apparent K_D curves (Figure 4e) show a roughly exponential increase with negative voltages. This results from the voltage dependence of both blocker binding and dissociation [7], which was also observed in other channels [17,18,46]. For TPrA, we recently demonstrated that the cause of the voltage dependency of k_{off} is electrostatic repulsion of the blocker by the ion occupation in binding site S4 in the selectivity filter [7].

For TPrA and TBA, the apparent K_D for Kcv$_S$ is significantly smaller (= higher affinity) than that for Kcv$_{NTS}$ (Figure 4e), especially at positive voltages. This result is surprising since it was expected that the additional cytosolic gate in Kcv$_S$ [2] might hinder the access of QAs to their binding site, which would result in a lower apparent affinity. The fact that we still detect differences in blocking in the open channel means that structural differences between the two isoforms

must cause additional changes at the cytosolic pore mouth and/or the cavity, which also affect the open channel. For a better characterization of such differences, the individual rate constants of blocker binding (k_{on}) and of release (k_{off}) were determined in addition to $K_D = k_{off}/k_{on}$. TPeA is the largest blocker that was tested with both isoforms. There is no significant difference in the K_D between Kcv$_{NTS}$ and Kcv$_S$.

Kinetic analysis of the fast blockers in Kcv$_{NTS}$ and Kcv$_S$

The reduced Markov model in Figure 1b is used to determine the rate constants of TPrA binding, k_{OB} (Figure 5a), and of blocker release, $k_{BO} = k_{off}$ (Figure 5b), for the open-state block. 0.1 mM TPrA has been applied to the cytosolic side of Kcv$_{NTS}$ (filled circles) and Kcv$_S$ (open circles), and the data are analyzed with extended beta distributions [32]. Regular (non-extended) beta distributions [47,48] have been used [17] for the block by TEA. In that study and in our previous work [7] as well as in Figure 5, both rate constants are voltage dependent.

The voltage dependency of k_{off} is somewhat stronger (factor of about 10 between −80 mV and +160 mV) than that of k_{on} (factor of about 5). The voltage dependence of k_{off} arises from the increase of K$^+$ occupancy at the binding site S4 in the selectivity filter in the blocked state [7] at negative
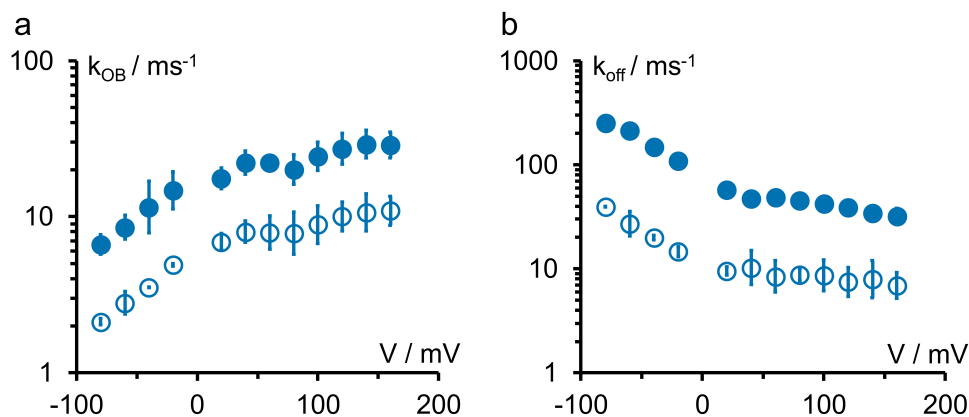
Figure 5. Kinetics of the open-state block with TPrA for the two channel isoforms Kcv$_{NTS}$ (filled symbols, no cytosolic gate) and Kcv$_S$ open symbols, with cytosolic gate) (Figure 2a,c). (a) Rate constant k_{OB} of blocker binding and (b) rate constant $k_{BO} = k_{off}$ of blocker release for 0.1 mM cytosolic TPrA. Averages ± sd of three experiments each. The small errors are a typical benefit of Kcv channels.

voltages. k_{on} decreases at negative voltages, presumably because the blocker has to move against the inward flow of ions in the unblocked state.

An interesting finding in Figure 5 is the parallel shift of the curves of k_{OB} (binding) and k_{off} (release) between those from Kcv_{NTS} and Kcv_S. This may indicate a change of the Eyring barriers for k_{on} and k_{off} as discussed below. Both rate constants are faster in Kcv_{NTS} than in Kcv_S at all voltages with a factor of about 3 for k_{OB} and about 5–8 for k_{off}. The larger influence of the channel isoform on k_{off} explains the difference in the apparent K_D in Figure 4e. A possible role of the residues involved in the cytosolic gate of Kcv_S [2] is investigated by the mutational studies below.

The fact that TEA affects both I_{app} and P_O (Figure 3) indicates a more complex blocking mechanism than for the other blockers. In contrast to all other phenomena observed in this work, the effect of TEA on P_O seems to be mostly voltage independent. Here, we only determine the kinetics of the fast TEA block, which is more comparable with that of the other blockers. The rate constants for TEA block were only determined for Kcv_{NTS} and are given in Figure S3.

Kinetic analysis of the slow blockers in Kcv_{NTS} and Kcv_S

For the slower blockers, TBA, TPeA, and THxA, dwell time analysis using the models in Figure 1d–f is employed, as illustrated in Figures 6–8. Representative dwell time histograms without blocker (control) and for the block of Kcv_{NTS} and Kcv_S by TPeA are shown in Figure 6 for +100 mV. The apparent open state O* is fitted by a single exponential function, the closed histograms with two (Kcv_{NTS}) or three (Kcv_S) exponential functions (Eq. 1, Figure 6). For Kcv_{NTS}, the blocked state B coincides with C_2 (Figure 6c), as obvious from the strong increase of the apparent C_2 with TPeA (dashed line); C_1 decreases because of mass conservation. In contrast, for Kcv_S, B coincides with C_3 (Figure 6d, dash-dotted line). Due to the increased number of "closed" events with the blocker, the mean duration of the open state is
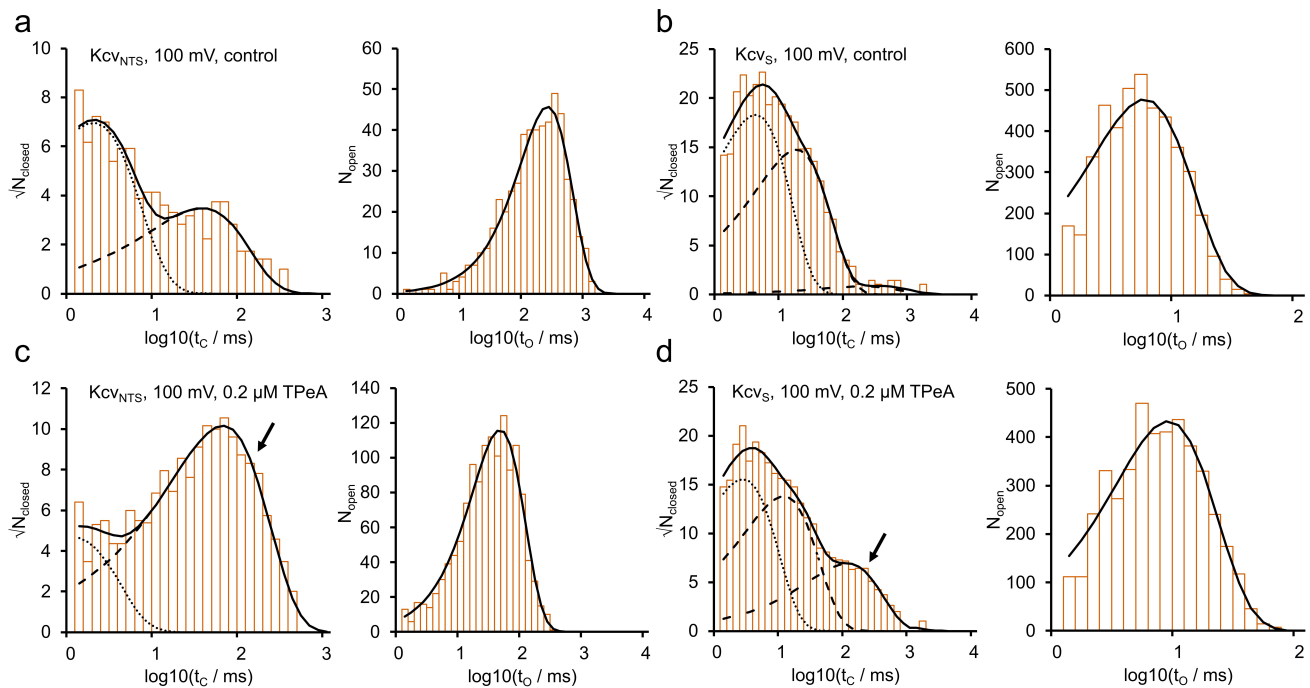
Figure 6. Dwell-time histograms of (a,c) Kcv_{NTS} and (b,d) Kcv_S under control conditions and blocked by TPeA. Exemplary closed- and open-time histograms at +100 mV for the control (a,b) and 200 nM TPeA (c,d). Open histograms (right hand side in each panel) were fitted by Eq. 1 (black) with a single exponential. Closed time histograms were fitted with a sum (black, continuous line) of two exponentials for Kcv_{NTS} or three exponentials for Kcv_S. Individual components: C_1 = dotted, C_2 = dashed, C_3 = dash-dot. Inclusion of state B in one of the closed states is indicated by the arrows.

shifted leftwards for Kcv_{NTS} (Figure 6a,c right-hand side). Because the blocking events are longer, but rarer in Kcv_S, the mean open duration is dominated by the intrinsic gating and not visibly affected by the blocker (Figure 6b,d right-hand side).

The voltage dependence of the occupation probabilities P is obtained from the time constants and amplitude factors of the individual exponential components in Figure 6 (Eq. 1) by means of Eq. 2. They are plotted in Figure 7. The TPeA-induced increases in C_2 in Kcv_{NTS} (Figure 7a–c) and in C_3 in Kcv_S (Figure 7d,e) are obvious. At negative voltages in Kcv_S, the effect of TPeA is too small to be detected (Figure 7f). Note that the respective C state (intrinsic gating) and state B (blocking) are not assumed to be mechanistically related, they have to be merged in the analysis because their dwell-times happen to coincide. They can be distinguished only by their concentration dependence.

Figures 6 and 7 show that at higher concentrations the TPeA block dominates either the C_2 (Kcv_{NTS}) or the C_3-component (Kcv_S). Thus, the rate constants for the respective closed state at concentrations higher than 100 nM (Kcv_{NTS}) and

200 nM (Kcv_S) were used as an approximation for the rate constants of open-state blocking (Figure 8). The threshold was set to a value at which the combined probability of B and the intrinsic closed state exceeds 10 times the probability of the closed state under control conditions. The same analysis was also done for TBA and THxA (Figure S4).

Whereas the ratio between Kcv_{NTS} and Kcv_S for both rate constants is in the order of 3 to 8 for TPrA (Figure 5), this difference decreases to a factor of 2 to 3 for TPeA (orange symbols in Figure 8). Since TPeA is larger than TPrA, this argues against the hypothesis that the causative difference between the two channels is a difference in pore diameter thus weakening the argument that the gate in Kcv_S decreases the pore diameter even in the open state. Further conclusions from the experiments in Figures 5–8 are discussed in the next section together with the data from the other blockers.

Role of blocker size in Kcv_{NTS}

To assess the kinetic origin of the size dependence of the apparent K_D in Figure 4e, we determine k_{on} and
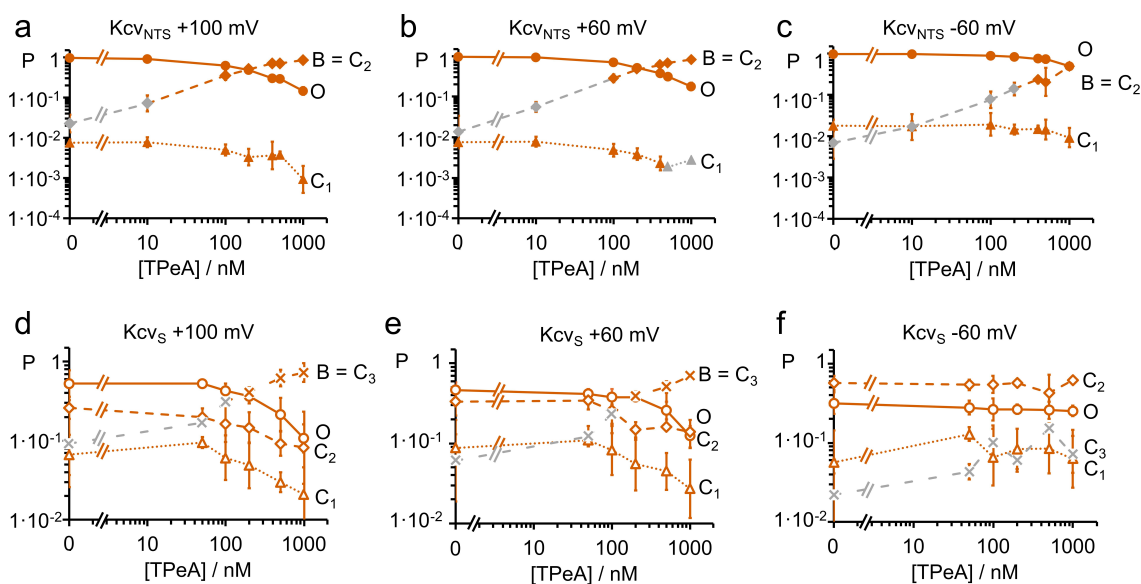
Figure 7. Dependence of occupation probabilities P of the states in the Markov models of Figure 1e or f on TPeA concentration. Association of the blocked state B to C_2 (diamonds in (a-c)) or C_3 (crosses in (d-f) is based on the dependence of their occupation probabilities on blocker concentration. The occupation probabilities of the open state (P_O, circles) and of the two or three closed states (P_{C1}, triangles, P_{C2}, diamonds, and P_{C3}, crosses) are shown for (a,b,c) Kcv_{NTS} (filled symbols) and for (d,e,f) Kcv_S (open symbols) at different TPeA concentrations at (a,d) +100 mV, (b,e) +60 mV and (c,f) −60 mV. Averages ± sd of three experiments each. Orange symbols in the curves related to B mark the concentrations, where the occupation probability of the respective state exceeds 10 times that of the control value and are therefore dominated by B. Grey symbols indicate that this probability is too small for the identification of B. for Kcv_S at −60 mV, and for both channels at −100 mV (not shown), this threshold was not reached (only gray symbols). The two additional gray triangles in B are data points, where due to the low probability of C_1, $n = 3$ could not be achieved for this state. This did not affect the determination of C_2.
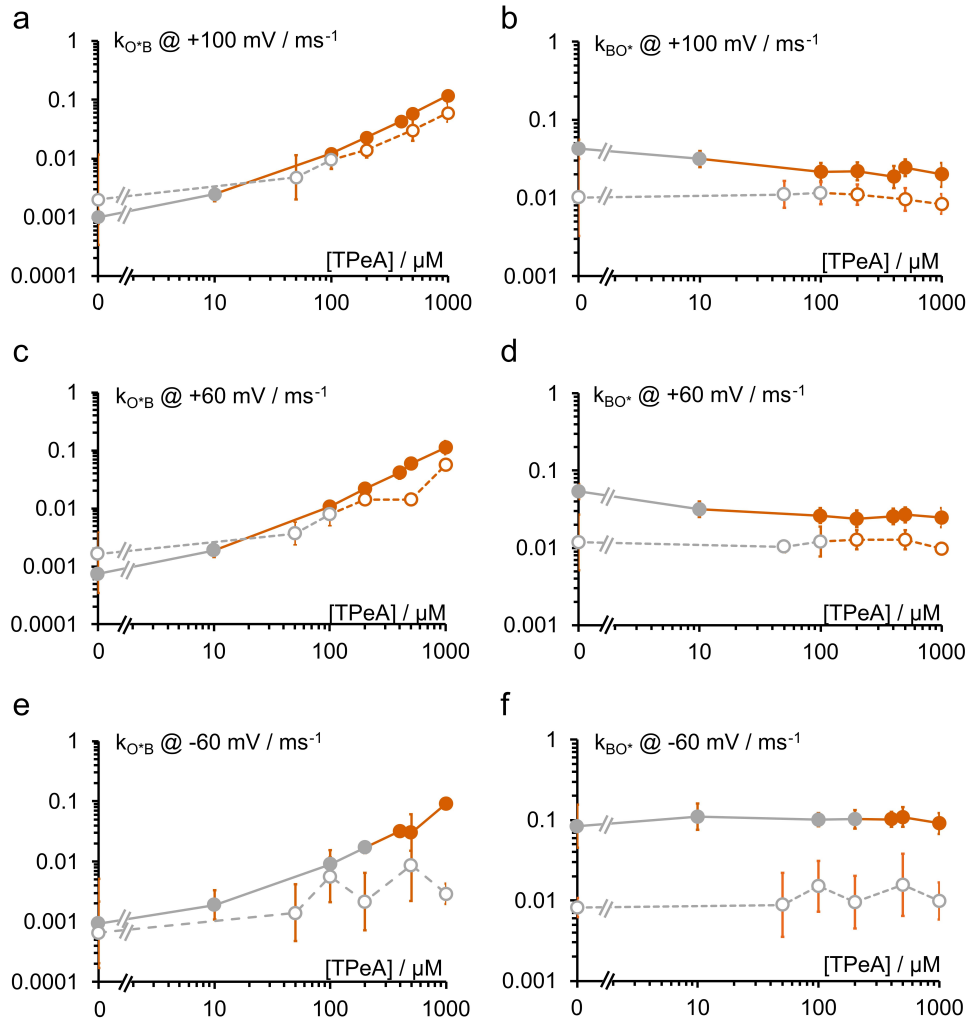
Figure 8. Rate constants of blocking of the open channel (a,c,e) k_{OB} and (b,d,f) k_{BO} as obtained from the dwell time histograms in Figure 6 by means of Eqs. 1 and 3 at −60 mV, +60 mV and +100 mV. Filled symbols: Kcv$_{NTS}$, open symbols; Kcv$_S$. Orange symbols are those where the blocked state B dominates the intrinsic closed state, and the rate constants can be taken as a good approximation of the rate constants of blocking. Grey symbols: this condition was not met; the rate constant was not used for further analysis. Mean ± sd of three experiments each.

k_{off} for all blockers (except for TMA, which is too fast to be analyzed even with extended beta distributions). Since k_{on} is defined as a concentration-independent parameter, it was calculated from k_{OB} by Eq. 6 with c being the blocker concentration.

$$k_{on} = \frac{k_{OB}}{c} \text{ or } k_{O*B} = k_{on} + \text{offset} \quad (6a, b)$$

For TEA and TPrA, Eq. 6a is applied to each individual experiment with subsequent averaging over all analyzed concentrations. In the case of TBA, TPeA, and THxA, state B is merged with one of the slow closed states of intrinsic gating resulting in $C_1^\star$, $C_2^\star$ or $C_3^\star$. Thus, the dependence of k_{O*B} on concentration is fitted with a linear equation (Eq. 6b); the offset accounts for the control values without blocker

(Figures 8a–e, leftmost data points). Merging the fast intrinsic states into O* (Figure 1d–f) does not influence the results of slow gating analysis. k_{on} determining the steepness of k_{O*B} of the graph in Figure 8 is averaged over all analyzed experiments. Also k_{off} is concentration-independent and is calculated by simply averaging k_{BO} or k$_{BO*}$ over all experiments and concentrations; limited to those concentrations and voltages where blocker dissociation can be reliably determined (e.g. orange data points in Figure 8b–f for TPeA).

Because of the voltage dependence of the block, a single concentration is often not enough to analyze the full voltage range. At negative voltages and low concentrations, the block is too weak, and at high concentrations at positive voltages, the block

is nearly complete, and not enough events can be detected. Since both k_{on} (Eq. 6a) and k_{off} are concentration-independent, pooling their values from different concentrations allows covering a larger voltage range [7].

Similar to Figure 5, the voltage dependence of k_{off} (Figure 9b) is slightly stronger than that of k_{on} (Figure 9a), particularly at negative voltages (Figure 9b) (Note that Figure 9a,c have a linear scale and Figure 9b,d a logarithmic scale). Figure 9b,d show that k_{off} changes exponentially by more than 4 orders of magnitude when the blocker size increases from 8 Å to 11 Å. This phenomenon originates in the higher hydrophobicity of the larger QAs [13,15,17] and causes the decrease of K_D with blocker size (Figure 4e).

k_{on} has been used to determine the accessible diameter of pores in other studies. In IRK1 and ROMK1 [18], the drop in k_{on} from TPrA to TBA was a factor of about 30, indicating that TBA was too large to properly enter. In contrast, we only observe a factor of 2 to 3 between TEA and TPrA or TBA and TPeA here, comparable with the drop between the small TEA and TPrA in IRK1 and ROMK1 [18]. This indicates that the cytosolic pore entrance (CPE) of Kcv_{NTS} is at least 11 Å wide.

Note that the diameters given in Figure 9 are approximations since the exact flexibility of the blockers [49,50] and of the protein is not known. For the sake of comparability, here we use the diameters as given in Figure 2b [44] as also used by other publications.

From the dependence of k_{on} on blocker size, a CPE diameter of ca. 9 Å was estimated for the inward rectifying K^+ channels IRK1 and ROMK1 [18]. Larger diameters of about 12 Å were reported for BK-like channels from rat muscle [17]. The closest bacterial homologue of BK channels, MthK also exhibits a very wide CPE of ca. 12 Å diameter, similar to the open-pore conformation of KcsA [19]; and K2P channels are still blocked by molecules as big as THxA (11 Å) [51]. Hence, the structure of the open CPE in Kcv appears to be more similar to that of channels cited in this second group.

Test of whether the blockers bind to the same binding site

The voltage dependence for k_{off} is very similar in both Kcv_{NTS} and Kcv_S for all blockers (parallel shift in Figure 9b). This voltage dependence is
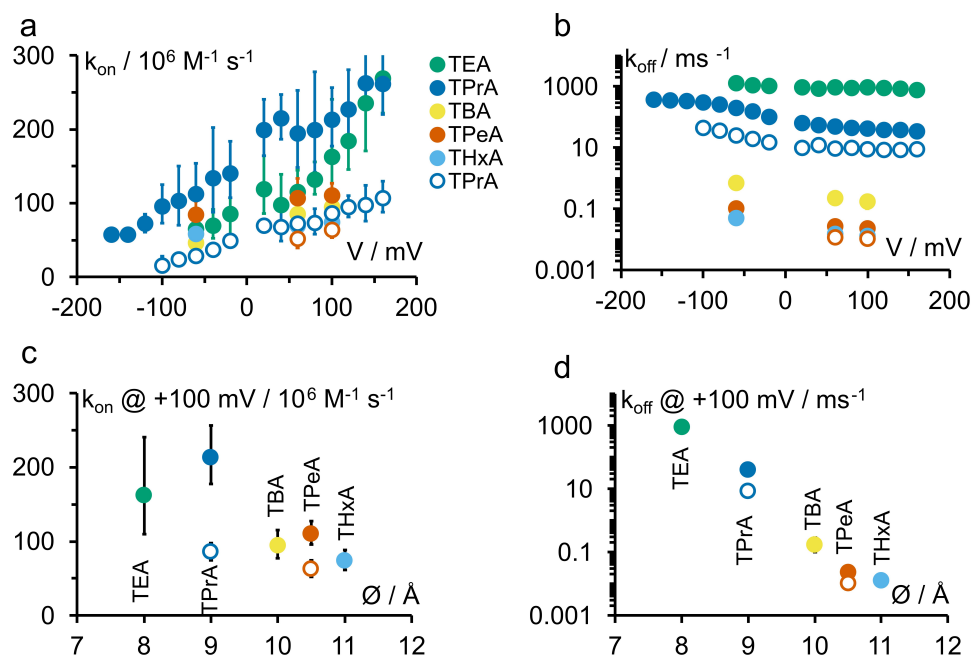

Figure 9. (a,b) Voltage dependence of the rate constants of open-state block (A) k_{on} as calculated by Eq. 6 and (B) k_{off} for different QAs. (c,d) Dependence of (C) k_{on} and (D) k_{off} at +100 mV on blocker diameter estimated by Robinson and Stokes [46]. Filled symbols: Kcv_{NTS}, open symbols: Kcv_S. Colors are defined in (A). Averages +/- sd of three experiments each.

used to address the question of whether the different blockers all bind to the same binding site in Kcv_{NTS}. First, for the comparison with other investigations in the literature, we fitted k_{off} with an exponential curve $k_{off} = k_{off,0} \cdot \exp(-z\delta \cdot FV/RT)$ (Figure 10a) even though k_{off} in this study is clearly not strictly exponential (Figures 9b, 10a). The resulting values of the effective valence $z\delta$ (TEA: 0.03 ± 0.04, TPrA: 0.23 ± 0.09, TBA: 0.16 ± 0.07, TPeA: 0.14 ± 0.12, THxA: 0.36 ± 0.05) are comparable to those in the literature (e.g. approx. 0.5 for TEA, TPrA, TBA, and TPeA in IRK1 and ROMK1 [18]). An ANOVA test shows that the effective valences $z\delta$ for TPrA, TBA, and TPeA in Kcv_{NTS} are indeed identical. The deviation of TEA can be explained by the unusual occurrence of two time constants. The deviation of THxA should not be overinterpreted, it might as well originate in the non-exponential shape of k_{off} and the different availability of sufficiently strong blocking effects at negative voltages for the different blockers.

In a previous work, we determined the correct equation of the voltage dependence of k_{off} for TPrA in Kcv_{NTS} [7]. The blocker is removed from its binding site by electrostatic repulsion by the K^+ ion at the S4 binding site. Importantly, the presence of the blocker does not disturb the K^+ distribution in the selectivity filter [7]. The curve shape is given by the ion occupation of binding site S4 in the 5-state model of ion hopping [52]. The equation for k_{off} includes the 10 rate constants of the 5-state ion hopping model [52], four of them being voltage-dependent. To decide whether

this mechanism, including the location of the binding site also holds for the other blockers, it is not necessary to repeat this intricate analysis. Instead, we compare the voltage dependence of the different k_{off} directly. The k_{off}-curve of TPrA was used as reference and normalized to the mean value at +100 mV. All other curves were then shifted by an adequate factor. This factor was determined by calculating the ratio of the mean values ($k_{off,other\ blocker}/k_{off,TPrA}$) for each voltage and then averaging over all voltages. Figure 10b shows a good coincidence of the shifted k_{off}. An ANOVA test reveals that the curves of TPrA, TBA, TPeA, and THxA coincide at +100 mV and +60 mV. For TPrA and THxA this is also true at −100 mV. Since TPrA and THxA are the blockers with the largest difference in diameter, we take these results as an indication that there is no serious difference of the voltage dependence of k_{off} for all four blockers, even though TBA and TPeA did not reach −100 mV. This is because the overlap of blocked and closed states makes dwell time analysis of the slow blockers challenging. This could also explain the minor deviation at −60 mV. TEA is not considered here because it has two different blocking mechanisms (Figure 3).

On a more "macroscopic" scale, the K_D values of all blockers for Kcv_{NTS} coincide when shifted in the same way. ANOVA indicates a high reliability of this coincidence (Figure 10c). In conclusion, it is very likely that the binding site is the same for TPrA, TBA, TPeA, and THxA and also the coupling between the K^+ ions at S4 and blocker dissociation k_{off} is the same.
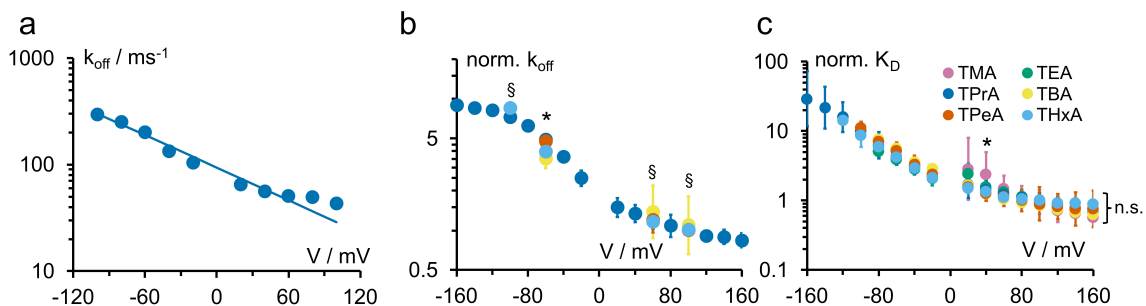
Figure 10. (a) Exemplary fit of k_{off} on an Kcv_{NTS} data set with 0.5 mM cytosolic TPrA with the equation $k_{off} = k_{off,0} \cdot \exp(-z\delta \cdot FV/RT)$, $z\delta = 0.28$, $k_{off,0} = 1.05 \cdot 10^5\ s^{-1}$. (b) Overlay of the normalized (see text) k_{off} for TPrA (dark blue), TBA (yellow), TPrA (orange) and THxA (light blue) in Kcv_{NTS}. §: No significant difference between the data points at this voltage. *: at least one data point is significantly different from the others. (c) Normalized (see text) K_D of all blockers in Kcv_{NTS}. A significant difference for at least one of the data points from the others is only found at +40 mV. One-parameter ANOVA with threshold $p = 0.05$.
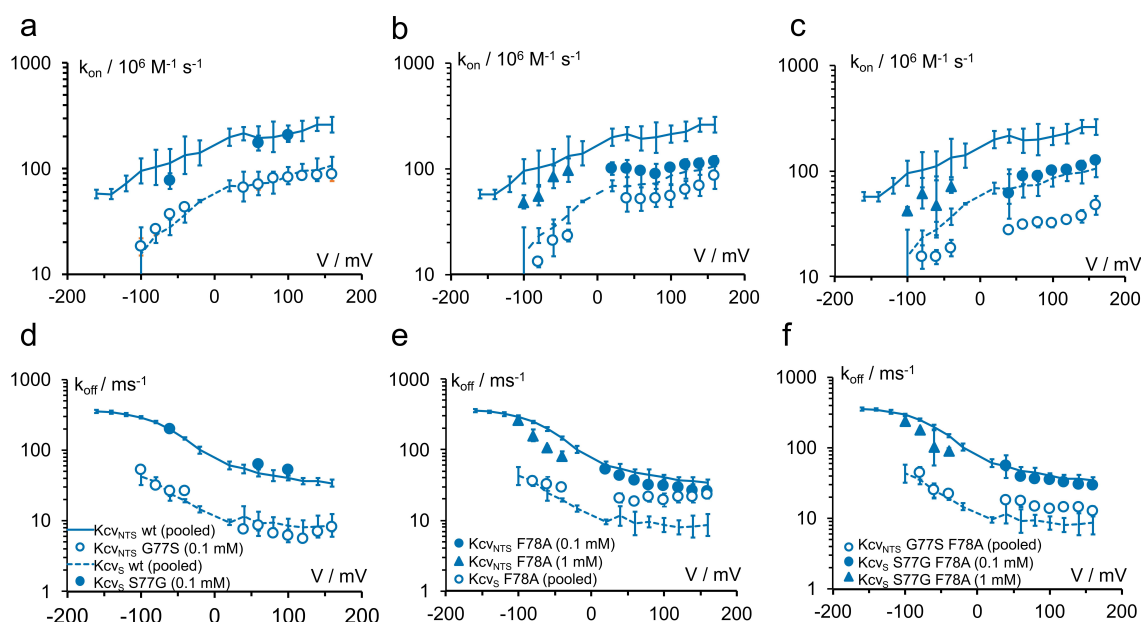
Influence of the residues on positions 77 and 78 on open-state blocking kinetics

Kcv$_S$ possesses a cytosolic gate, which is absent in Kcv$_{NTS}$ (Figure 2a,c) [2]. This gate consists of an unusual mechanism. It does not form a bundle crossing; instead, a hydrogen bond between the S77 side chain on TM2 and the backbone carbonyl of I73 controls the positioning of the side chain of F78, which can occlude the pathway for ions at the CPE. The phenylalanine is also present in Kcv$_{NTS}$, but a glycine at position 77 instead of the serine causes the gate to be constitutively open. The S77G/G77S mutations switch the gating phenotypes of the two channels, both for the slow cytosolic gate (state C$_3$ [2]) and the second component of O-M gating (state M in the Markov models, Figure 1) visible only at positive voltages. The voltage-dependent component at negative voltages is identical in both isoforms (Figure S5). The single-channel current is not affected (Figure S7).

In order to investigate whether the residues forming the cytosolic gate are responsible for the differences in the TPrA block in Kcv$_{NTS}$ and Kcv$_S$, we determined the rate constants k_{on} and k_{off} of the open state block in Kcv$_{NTS}$, Kcv$_S$ and for several mutations at the cytosolic gate.

Compared to Kcv$_{NTS}$, k_{on} and k_{off} are decreased both in Kcv$_S$ (Figure 5) and in the mutant Kcv$_{NTS}$ G77S (which introduces the gate into Kcv$_{NTS}$) (Figure 11a,d open circles). The decrease of k_{off} is stronger than that of k_{on} thus leading to a decrease in K_D. In the reverse case, the mutant Kcv$_S$ S77G shows the same blocking rate constants as Kcv$_{NTS}$ (Figure 11a,d filled circles). This result seems to support the hypothesis that the bulky side chain of F78 also in the open state is in a position where it hinders access and release of the blocker, as long as the second component of the gate, S77, is also present.

However, this simple picture is destroyed when the mutation F78A comes into play. The side chain of alanine is too small to hinder blocker access or release. Therefore, the elimination of

Figure 11. Block by TPrA. Influence of the residues at positions 77 and 78 on the rate constants of (a, b, c) blocker binding $k_{on} = k_{OB}$ /[TPrA]) and (d,e,f) release ($k_{BO} = k_{off}$) in different mutants of Kcv$_{NTS}$ and of Kcv$_S$. Lines show the wild-type data (Kcv$_{NTS}$: continuous, Kcv$_S$: dashed), the symbols indicate the residue at locations 77: G = filled, S = open for the mutants (a,d) S77G and G77S (b,e) F78A and (c,f) the double mutants. "pooled:" wt data averaged over TPrA concentration from 0.05 – 5 mM (Kcv$_{NTS}$) and 0.1 – 1 mM (Kcv$_S$), data for Kcv$_{NTS}$ S77G F78A averaged over 0.1 & 1 mM. All other blocker concentrations are indicated in the legends. All data points: mean ± sd of at least three experiments each. Because of the decrease of the signal with higher negative voltages, rate constants could not be determined from fitting amplitude histograms for voltages more negative than −80 mV or −60 mV for all mutants and Kcv$_S$.

the phenylalanine side chain by replacing F with A "should" increase k_{on} and k_{off}. However, Figure 11b,c show that even the opposite effect occurs in the case of k_{on}. With both serine (Kcv$_{NTS}$ G77S F78A and Kcv$_S$ F78A) and glycine (Kcv$_{NTS}$ F78A and Kcv$_S$ S77G F78A), k_{on} is reduced by the F78A mutation.

In the case of k_{off}, the elimination of the phenylalanine side chain in Kcv$_S$ leads to a small increase, which even reaches the k_{off} of Kcv$_{NTS}$ at high positive voltages (Figure 11e). The increase of k_{off} with S on position 77 is much smaller in the double mutant Kcv$_{NTS}$ G77S F78A (Figure 11f).

Conclusion

The accessibility studies above with blockers of different size have determined a lower bound for the width of the path from the cytosol to the entrance of the selectivity filter in Kcv$_{NTS}$: at least 11 Å (Figure 9). In previous electrophysiological studies on ion dynamics in the selectivity filter of Kcv$_{NTS}$ diffusion limitation at the cytosolic pore entrance was neglected without any experimental evidence [3,7]. Now, the experimentally determined minimal CPE diameter verifies that the CPE is wide enough not to pose any significant diffusion limitation for K$^+$ ions. This information can also provide a useful additional constraint for future structural models in addition to those that have been already used successfully [2,7–9].

Aside from being a good model system, Kcv channels are a possible future target for molecules preventing virus spreading in alga cultures. This work investigates the cytosolic pore mouth, which is not easily accessible (assuming the channels are oriented in the virus in the same way as in heterologous expression systems). However, any biophysical information about a potential drug target might be useful someday. Kcv$_{PBCV-1}$ from a different *chlorella* virus has an external binding site for TEA [53] and might be an even more interesting target.

Diffusion limitations and/or pore diameter restrictions by bulky amino acids have been studied in different channels [20,21]. Kopec and colleagues [54] found that changes in the diameter of the CPE of MthK did not prohibit K$^+$ movement. Similarly, in Kcv$_{NTS}$, in the case of k_{on} in this study, the results

in Figure 11b,c clearly rule out the involvement of diffusion limitation by the phenylalanine on position 78, since its replacement by alanine decreases and does not increase k_{on}.

The increase of k_{off} in the mutant F227A (roughly corresponding to F78A in Kcv here) in the bacterial Na$^+$ channel has been called trapping [55], i.e. the phenylalanine hinders the dissociation of the blocker. This trapping (or lack thereof) has often been used to identify the location of a gate [10,11]. However, in Figure 11d,e, the increase of k_{off} in F78A is zero or very small at negative voltages (Figure 11e) or strongly voltage-dependent at positive voltages (Figure 11d). Thus, a minor participation of trapping cannot be excluded, but another mechanism not based on the phenylalanine is the alternative or at least the dominating origin of the effect of the mutants on k_{off}.

Such a hypothetical mechanism could be a change in conformation or hydrophobicity near the binding site of the blocker. It is well documented, that the binding of QAs to the potassium channel pore is mostly due to hydrophobic interactions, e.g [15]. The aforementioned hypothesis is supported by the fact that, also the voltage-independent component of k_{OM} of intrinsic gating at positive voltages, called $k_{OM,2}$ is influenced by the S-G mutations, but not by mutations at position 78 (Figure S5). Thus, the binding site for blocker and the (currently still unknown) site controlling $k_{OM,2}$ seem to be in nearby positions of the protein but are not identical. Even though the mutations at position 77 influence both blocking and $k_{OM,2}$ (Figure 11 and Figure S5) the blockers have no influence on voltage-dependent O-M gating at negative voltages (Figure S5 for TPrA and Figure S6 for TBA). This supports our previous findings that the blocker does not disturb the ion occupation in the selectivity filter, as verified by 3D reference interaction site model (3D RISM) calculation [7].

If the mutations at positions 77 and 78 both influence the binding kinetics, then the question comes up of whether they act on the same Eyring barrier for the blocking kinetics. Such a concerted action on an Eyring barrier for channel gating has been found to influence the number of subunits with the mutation

S42T on k_{OM} [56]. In Table S2, an additive contribution of both mutations in Figure 11 to the height of the energy barrier (as indicated by the product of the ratios of the rate constants) for the rate constants of blocker kinetics is found only for k_{on} and only when Kcv_{NTS} wt provides the protein background. In all other cases, the double mutations do not contribute in such an additive manner to the energy barrier, indicating that the effects caused by the single mutations in these three cases are energetically not independent [57] or act on different parts of the protein.

Disclosure statement

No potential conflict of interest was reported by the author(s).

Author contributions

TK, TSG, OR, and ND performed experiments and analyzed data. UPH analyzed the data and wrote the manuscript. IS designed research, analyzed data, and wrote the manuscript. All authors edited the manuscript.

Data availability statement

Materials and data created in this work as well as the program bownhill are available upon reasonable request.

ORCID

Indra Schroeder 🄳 http://orcid.org/0000-0002-7875-983X

References

[1] Thiel G, Baumeister D, Schroeder I, et al. Minimal art: or why small viral K+ channels are good tools for understanding basic structure and function relations. Biochim Biophys Acta. 2011;1808(2):580–588. doi: 10.1016/j.bbamem.2010.04.008

[2] Rauh O, Urban M, Henkes LM, et al. Identification of intrahelical bifurcated H-Bonds as a new type of gate in K+ channels. J Am Chem Soc. 2017;139 (22):7494–7503. doi: 10.1021/jacs.7b01158

[3] Rauh O, Hansen U-P, Scheub DD, et al. Site-specific ion occupation in the selectivity filter causes voltage-dependent gating in a viral K+ channel. Sci Rep. 2018;8(1):10406. doi: 10.1038/s41598-018-28751-w

[4] Eckert D, Schulze T, Stahl J, et al. A small viral potassium ion channel with an inherent inward rectification. Channels Austin Tex. 2019;13(1):124–135. doi: 10.1080/19336950.2019.1605813

[5] Kang M, Graves M, Mehmel M, et al. Genetic diversity in chlorella viruses flanking kcv, a gene that encodes a potassium ion channel protein. Virology. 2004;326:150–159. doi: 10.1016/j.virol.2004.05.023

[6] Winterstein L-M, Kukovetz K, Hansen U-P, et al. Distinct lipid bilayer compositions have general and protein-specific effects on K+ channel function. J Gen Physiol. 2021;153(2). doi: 10.1085/jgp.202012731

[7] Gabriel TS, Hansen U, Urban M, et al. Asymmetric interplay between K+ and blocker and atomistic parameters from physiological experiments quantify K+ channel blocker release. Front Physiol. 2021;12. doi: 10.3389/fphys.2021.737834

[8] Tayefeh S, Kloss T, Kreim M, et al. Model development for the viral kcv potassium channel. Biophys J. 2009;96 (2):485–498. doi: 10.1016/j.bpj.2008.09.050

[9] Andersson AEV, Kasimova MA, Delemotte L. Exploring the viral channel KcvPBCV-1 function via computation. J Membr Biol. 2018;251(3):419–430. doi: 10.1007/s00232-018-0022-2

[10] Posson DJ, McCoy JG, Nimigean CM. The voltage-dependent gate in MthK potassium channels is located at the selectivity filter. Nat Struct Mol Biol. 2013;20(2):159–166. doi: 10.1038/nsmb.2473

[11] Posson DJ, Rusinova R, Andersen OS, et al. Calcium ions open a selectivity filter gate during activation of the MthK potassium channel. Nat Commun. 2015;6 (1):8342. doi: 10.1038/ncomms9342

[12] Piechotta PL, Rapedius M, Stansfeld PJ, et al. The pore structure and gating mechanism of K2P channels. Embo J. 2011;30(17):3607–3619. doi: 10.1038/emboj.2011.268

[13] Armstrong CM. Interaction of tetraethylammonium ion derivatives with the potassium channels of giant axons. J Gen Physiol. 1971;58(4):413–437. doi: 10.1085/jgp.58.4.413

[14] Lenaeus MJ, Vamvouka M, Focia PJ, et al. Structural basis of TEA blockade in a model potassium channel. Nat Struct Mol Biol. 2005;12(5):454–459. doi: 10.1038/nsmb929

[15] Lenaeus MJ, Burdette D, Wagner T, et al. Structures of KcsA in complex with symmetrical quaternary ammonium compounds reveal a hydrophobic binding site. Biochemistry. 2014;53(32):5365–5373. doi: 10.1021/bi500525s

[16] French RJ, Shoukimas JJ. Blockage of squid axon potassium conductance by internal tetra-N-alkylammonium ions of various sizes. Biophys J. 1981;34(2):271–291. doi: 10.1016/S0006-3495(81)84849-7

[17] Villarroel A, Alvarez O, Oberhauser A, et al. Probing a Ca^{2+}-activated K^+ channel with quaternary ammonium ions. Pflugers Arch. 1988;413(2):118–126. doi: 10.1007/BF00582521

[18] Guo D, Lu Z. Kinetics of inward-rectifier K+ channel block by quaternary alkylammonium ions: dimension and properties of the inner pore. J Gen Physiol. 2001;117(5):395–406. doi: 10.1085/jgp.117.5.395

[19] Jiang Y, Lee A, Chen J, et al. The open pore conformation of potassium channels. Nature. 2002;417 (6888):523–526. doi: 10.1038/417523a

[20] Langan PS, Vandavasi VG, Kopec W, et al. The structure of a potassium-selective ion channel reveals a hydrophobic gate regulating ion permeation. IucrJ. 2020;7(5):835–843. doi: 10.1107/S2052252520008271

[21] Whicher JR, MacKinnon R. Structure of the voltage-gated K+ channel Eag1 reveals an alternative voltage sensing mechanism. Science. 2016;353 (6300):664–669. doi: 10.1126/science.aaf8070

[22] Xue J, Han Y, Zeng W, et al. Structural mechanisms of gating and selectivity of human rod CNGA1 channel. Neuron. 2021;109(8):1302–1313.e4. doi: 10.1016/j.neuron.2021.02.007

[23] Braun CJ, Lachnit C, Becker P, et al. Viral potassium channels as a robust model system for studies of membrane–protein interaction. Biochim Biophys Acta. 2013;1838(4):1096–1103. doi: 10.1016/j.bbamem.2013.06.010

[24] Papworth C, Bauer JC, Braman J, et al. Site-directed mutagenesis in one day with >80 % efficiency. Strategies. 1996;9:3–4.

[25] Winterstein L-M, Kukovetz K, Rauh O, et al. Reconstitution and functional characterization of ion channels from nanodiscs in lipid bilayers. J Gen Physiol. 2018;150(4):637–646. doi: 10.1085/jgp.201711904

[26] Braun CJ, Baer T, Moroni A, et al. Pseudo painting/air bubble technique for planar lipid bilayers. J Neurosci Methods. 2014;233:13–17. doi: 10.1016/j.jneumeth.2014.05.031

[27] Montal M, Mueller P. Formation of bimolecular membranes from lipid monolayers and a study of their electrical properties. Proc Natl Acad Sci USA. 1972;69 (12):3561–3566. doi: 10.1073/pnas.69.12.3561

[28] Gazzarrini S, Kang M, Abenavoli A, et al. Chlorella virus ATCV-1 encodes a functional potassium channel of 82 amino acids. Biochem J. 2009;420(2):295–305. doi: 10.1042/BJ20090095

[29] Rauh O, Hansen U-P, Mach S, et al. Extended beta distributions open the access to fast gating in bilayer experiments—assigning the voltage-dependent gating to the selectivity filter. FEBS Lett. 2017;591 (23):3850–3860. doi: 10.1002/1873-3468.12898

[30] Heinemann SH, Sigworth FJ. Open channel noise. VI. Analysis of amplitude histograms to determine rapid kinetic parameters. Biophys J. 1991;60(3):577–587. doi: 10.1016/S0006-3495(91)82087-2

[31] Hille B. Ion channel excitable membranes. Sunderland Mass. USA: Sinauer Associates, Inc.; 2001.

[32] Schroeder I. How to resolve microsecond current fluctuations in single ion channels: the power of beta distributions. Channels. 2015;9(5):262–280. doi: 10.1080/19336950.2015.1083660

[33] Schroeder I, Hansen U-P. Strengths and limits of beta distributions as a means of reconstructing the true single-channel current in patch clamp time series with fast gating. J Membr Biol. 2006;210(3):199–212. doi: 10.1007/s00232-006-0858-8

[34] Albertsen A, Hansen U-P. Estimation of kinetic rate constants from multi-channel recordings by a direct fit of the time series. Biophys J. 1994;67(4):1393–1403. doi: 10.1016/S0006-3495(94)80613-7

[35] Caceci MS, Cacheris WP. Fitting curves to data - the simplex algorithm is the answer. BYTE. 1984;5:340–362.

[36] Schroeder I, Hansen U-P. Using a five-state model for fitting amplitude histograms from MaxiK channels: β-distributions reveal more than expected. Eur Biophys J. 2009;38(8):1101–1114. doi: 10.1007/s00249-009-0515-0

[37] Schroeder I, Hansen U-P. Interference of shot noise of open-channel current with analysis of fast gating: patchers do not (yet) have to care. J Membr Biol. 2009;229(3):153–163. doi: 10.1007/s00232-009-9183-3

[38] Schultze R, Draber S. A nonlinear filter algorithm for the detection of jumps in patch-clamp data. J Membr Biol. 1993;132(1):41–52. doi: 10.1007/BF00233050

[39] Tewes N, Kubitzki B, Bytyqi F, et al. Mutation in pore-helix modulates interplay between filter gate and Ba2+ block in a Kcv channel pore. J Gen Physiol. 2024;156(5):e202313514. doi: 10.1085/jgp.202313514

[40] Blunck R, Kirst U, Riessner T, et al. How powerful is the dwell-time analysis of multichannel records? J Membr Biol. 1998;165(1):19–35. doi: 10.1007/s002329900417

[41] Yohannan S, Hu Y, Zhou Y. Crystallographic study of the tetrabutylammonium block to the KcsA K^+ channel. J Mol Biol. 2007;366(3):806–814. doi: 10.1016/j.jmb.2006.11.081

[42] Bordoli L, Kiefer F, Arnold K, et al. Protein structure homology modeling using SWISS-MODEL workspace. Nat Protoc. 2009;4(1):1–13. doi: 10.1038/nprot.2008.197

[43] Pettersen EF, Goddard TD, Huang CC, et al. UCSF chimera—A visualization system for exploratory research and analysis. J Comput Chem. 2004;25 (13):1605–1612. doi: 10.1002/jcc.20084

[44] Robinson RA, Stokes RH. Electrolyte solutions. London: Butterworths; 1959.

[45] Wong B. Points of view: color blindness. Nat Methods. 2011;8(6):441–441. doi: 10.1038/nmeth.1618

[46] Oliver D, Hahn H, Antz C, et al. Interaction of permeant and blocking ions in cloned inward-rectifier K^+ channels. Biophys J. 1998;74(5):2318–2326. doi: 10.1016/S0006-3495(98)77941-X

[47] FitzHugh R. Statistical properties of the asymmetric random telegraph signal, with applications to

single-channel analysis. Math Biosci. 1983;89(1):75–89. doi: 10.1016/0025-5564(83)90028-7

[48] Yellen G. Ionic permeation and blockade in Ca^{2+}-activated K^+ channels of bovine chromaffin cells. J Gen Physiol. 1984;84(2):157–186. doi: 10.1085/jgp.84.2.157

[49] Faraldo-Gómez JD, Kutluay E, Jogini V, et al. Mechanism of intracellular block of the KcsA K^+ channel by tetrabutylammonium: insights from X-ray crystallography, electrophysiology and replica-exchange molecular dynamics simulations. J Mol Biol. 2007;365(3):649–662. doi: 10.1016/j.jmb.2006.09.069

[50] O'Leary ME, Kallen RG, Horn R. Evidence for a direct interaction between internal tetra-alkylammonium cations and the inactivation gate of cardiac sodium channels. J Gen Physiol. 1994;104(3):523–539. doi: 10.1085/jgp.104.3.523

[51] Schewe M, Sun H, Mert Ü, et al. A pharmacological master key mechanism that unlocks the selectivity filter gate in K+ channels. Science. 2019;363(6429):875–880. doi: 10.1126/science.aav0569

[52] Bernèche S, Roux B. A gate in the selectivity filter of potassium channels. Struct Lond Engl. 1993;13 (2005):591–600. doi: 10.1016/j.str.2004.12.019

[53] Tan Q, Ritzo B, Tian K, et al. Tuning the tetraethylammonium sensitivity of potassium channel kcv by subunit combination. J Gen Physiol. 2012;139 (4):295–304. doi: 10.1085/jgp.201110725

[54] Kopec W, Rothberg BS, de Groot BL. Molecular mechanism of a potassium channel gating through activation gate-selectivity filter coupling. Nat Commun. 2019;10 (1):1–15. doi: 10.1038/s41467-019-13227-w

[55] Shimomura T, Irie K, Fujiyoshi Y. Molecular determinants of prokaryotic voltage-gated sodium channels for recognition of local anesthetics. FEBS J. 2016;283 (15):2881–2895. doi: 10.1111/febs.13776

[56] Rauh O, Opper J, Sturm M, et al. Role of ion distribution and energy barriers for concerted motion of subunits in selectivity filter gating of a K+ channel. J Mol Biol. 2022;434(9):167522. doi: 10.1016/j.jmb.2022.167522

[57] Horovitz A. Double-mutant cycles: a powerful tool for analyzing protein structure and function. Fold Des. 1996;1(6):R121–R126. doi: 10.1016/S1359-0278(96)00056-9